

LEARNING DYNAMICALLY INSPIRED INVARIANT SUBSPACES FOR KOOPMAN AND TRANSFER OPERATOR APPROXIMATION

GARY FROYLAND* AND KEVIN KÜHL*

Abstract. Transfer and Koopman operator methods offer a framework for representing complex, nonlinear dynamical systems via linear transformations, enabling a deeper understanding of the underlying dynamics. The spectra of these operators provide important insights into system predictability and emergent behaviour, although efficiently estimating them from data can be challenging. We approach this issue through the lens of general operator and representational learning, in which we approximate these linear operators using efficient finite-dimensional representations. Specifically, we machine-learn orthonormal basis functions that are dynamically tailored to the system. This learned basis provides a particularly accurate approximation of the operator’s action as well as a nearly invariant finite-dimensional subspace. We illustrate our approach with examples that showcase the retrieval of spectral properties from the estimated operator, and emphasise the dynamically adaptive quality of the machine-learned basis.

Key words. Koopman Operator, Transfer Operator, Invariant Subspace, Spectrum

1. Introduction. Nonlinear dynamical systems emerge in a variety of domains, including biology, ecology, physics, and engineering; understanding their behaviour is critical for prediction and control. However, studying nonlinear systems is difficult due to their complex and frequently high-dimensional and chaotic behaviour. A promising approach is to study a *nonlinear* system via an associated *linear* operator acting on observables (*nonlinear functions* of the state). In this operator-theoretic framework, the nonlinear evolution in state space is lifted to a linear (but infinite-dimensional) evolution in a function space. For example, given a discrete dynamical system $x_{n+1} = T(x_n)$ with state space X , one can define the transfer operator \mathcal{L} acting on a function $g : X \rightarrow \mathbb{R}$ by composition:

$$\mathcal{L}g := g \circ T^{-1}.$$

The operator $\mathcal{L} : L^2(X) \rightarrow L^2(X)$ is linear even if T is nonlinear. By analysing \mathcal{L} , one can leverage linear techniques to understand nonlinear dynamics [11, 28, 12, 10, 19]. The trade-off is that \mathcal{L} typically acts on infinite-dimensional function spaces, and to study \mathcal{L} in practice we must work with finite-dimensional approximations.

A major challenge in typical applications is that we do not know *a priori* which observables or subspaces will yield a good finite-dimensional representation of \mathcal{L} . Many traditional approaches assume a predefined set of basis functions — e.g. monomials, Fourier modes, or the library of observables supplied to Extended Dynamic Mode Decomposition (EDMD) [34] — that may not be well suited to the system at hand. For example, data-driven approximations of the Koopman operator, such as DMD [31, 2] and its variations, depend on the user supplying observables that span a subspace that is approximately invariant under \mathcal{L} . If key observables are omitted, important dynamics can be missed, while a lack of invariance can contribute to estimation errors. Consequently, identifying coordinate transformations or feature spaces in which a nonlinear system behaves linearly remains an active and widely researched topic [21, 1, 13, 23].

Several approaches attempt to learn such coordinate transformations. Brunton *et al.* consider a sparse dictionary of functions with fixed form to obtain a finite

*School of Mathematics and Statistics, UNSW Sydney, Sydney NSW 2052, Australia. (g.froyland@unsw.edu.au, k.kuhl.oliveira@unsw.edu.au).

Koopman-invariant subspace for control [7]. Starting from a specially structured dictionary, Johnson *et al.* [17] are able to construct invariant subspaces and, in a companion work, propose a test for their invariance [18]. Turning to the use of neural networks, Li *et al.* [24] employ a neural dictionary (neural networks as functions), updating the basis and Koopman matrix separately. As a result, operator errors never backpropagate into the dictionary, and the learned observables are not adapted to the underlying dynamics.

Unifying both operator and embedding learning, Otto and Rowley’s linearly recurrent autoencoder network (LRAN) forces an encoded version of the state space to evolve linearly in a Koopman-invariant subspace [29]. However, the loss is skewed towards a good reconstruction of the state space from its encoded version. The network is tuned to embed the state space compactly rather than to learn a function space that is nearly closed under \mathcal{L} . Other encoder-decoder schemes, such as Yeung *et al.* [35] and control-oriented work by [32] follow a similar approach. Takeishi *et al.* [33] also learn observables by minimizing a one-step residual; at the global optimum these observables span an invariant subspace. Using a modified autoencoder structure, Lusch, Brunton, and Kutz consider the spectrum of the operator and learn Koopman eigenfunctions [27], but tuning the network parameters is not straightforward.

In parallel, there has been significant progress in learning nonlinear operators (nonlinear maps between function spaces) with neural networks. This work is built upon the universal approximation theorem for operators [8, 22], which extends the classic universal approximation property of neural nets from finite-dimensional functions to infinite-dimensional functionals. Lu *et al.* [26] have proposed the Deep Operator Network (DeepONet) architecture. DeepONet consists of two subnetworks (a branch network that encodes the input function via evaluations at a fixed set of sensor points, and a trunk network that encodes the location where the output is evaluated) and can learn nonlinear operator mappings. Another example is the Basis Operator Network (BasisONet) of Hua and Lu [16], which uses a neural-network-based dual autoencoder setting to learn a lower-dimensional representation (basis) for functions in the input and output function spaces. Over the past few years, different architectures have been proposed for various scenarios, including Fourier Neural Operators [25], and PCA-Net [3]. A comprehensive review of operator learning techniques may be found in [4], including insightful parallels to the matrix recovery problem.

In this current work we take the BasisONet architecture as a starting point, and exploit properties of Perron–Frobenius and Koopman operators to reduce the number of encoding blocks and produce a *single basis of functions that span an invariant subspace*. Our Single Autoencoder Basis Operator Network (SABON) learns a basis with no predefined functional form and trains it with a relative L^2 loss. For every training observable we minimise a residual measuring how well a finite matrix represents \mathcal{L} on the subspace spanned by the learned basis. Because of the inner-product structure of our projection block, gradient descent methods naturally push the basis toward orthogonality, improving numerical conditioning. An optional sparsity penalty encourages local support (Example 1). The combined learning of both the operator estimate and the collection of functions produces a basis that is adapted to the underlying dynamics, which further enhances the invariance property (Example 2).

An outline of the paper is as follows. Section 2 introduces the Single Autoencoder Basis Operator Network (SABON) and proves a universal-approximation theorem for the presented setting. Section 3 first validates SABON on a circle rotation map, and shows that spectral properties of the transfer operator can be recovered from the learned basis and approximator. Next, we apply SABON to a nonlinear hyperbolic

map of the 2-torus, and demonstrate that the learned basis adapts to the strongly anisotropic dynamics and outperforms an equal-cardinality Fourier basis in terms of basis invariance and eigenfunction approximation. The final section discusses our main findings and sketches directions for future work.

2. Methodology. Let $X \subset \mathbb{R}^d$ denote a compact, metrizable space of intrinsic dimension $d' \leq d$, where elements of X are parameterised by d -tuples of real numbers. The set X is the domain of our nonlinear dynamics, which are generated by the map $T: X \rightarrow X$. We assume that \mathcal{L} is continuous; sufficient conditions on T ensuring this continuity are given in Remark 2.2. Let $\{x_i\}_{i=1,\dots,n} \subset X$ be a set of sample points representing a discretization of the state space. We assume that in the large-data limit these sample points are distributed according to a probability measure ν on X , and in what follows we consider the space of square-integrable real-valued functions $L^2(X, \nu)$, which we write as $L^2(X)$ for brevity. An observable $g \in L^2(X)$ is represented by its values on this grid, that is $[g(x_1), g(x_2), \dots, g(x_n)]^\top$. The action of the transfer operator produces a new function $\mathcal{L}(g)$, whose values on the grid are $[(\mathcal{L}g)(x_1), \dots, (\mathcal{L}g)(x_n)]^\top$. If $V \subset L^2(X)$ is a finite-dimensional invariant subspace spanned by basis functions ϕ_1, \dots, ϕ_N , then the restriction of \mathcal{L} to V can be represented by an $N \times N$ matrix L such that $\mathcal{L}\phi_j = \sum_{k=1}^N L_{kj}\phi_k$. If V is not \mathcal{L} -invariant, a finite-rank approximation $\hat{\mathcal{L}}$ is often obtained by first applying \mathcal{L} to the basis elements of V and then projecting the resulting functions back into V . The quality of this approximation depends on the choice of subspace V . Two important contributors to approximation accuracy are the richness of the space V and the error incurred due to projection into V . The latter error is greatly reduced if V is approximately invariant under \mathcal{L} . Invariant (or approximately invariant) subspaces thus play a key role in accurately approximating \mathcal{L} .

In preparation for the neural learning, we suppose that the state space X may be embedded in \mathbb{R}^d . We will adopt the standard convention of scalar feed-forward neural networks as a composition of affine maps and nonlinear activations, $\phi: \mathbb{R}^d \rightarrow \mathbb{R}$. Stacking N such networks gives a vector-valued network $\hat{\phi}(x): \mathbb{R}^d \rightarrow \mathbb{R}^N$, written as

$$(2.1) \quad \hat{\phi}(x) = (\phi_1(x), \dots, \phi_N(x))^\top$$

Finally, we call the collection $\{\phi_1, \dots, \phi_N\}$ a *neural basis* for the finite-dimensional subspace $V = \text{span}\{\phi_j\}_{j=1}^N \subset L^2(X)$.

2.1. Single Autoencoder Basis Operator Networks (SABON). To address the problem of simultaneously learning an approximator to the Transfer Operator and a suitable invariant subspace, we employ an architecture comprising four stages: (i) an encoder \mathcal{E} that constructs basis functions evaluated on a training grid, (ii) a block \mathcal{P} that projects observables onto the learned basis, (iii) a linear latent map \mathcal{G} that approximates the transfer operator in the coefficient space, and (iv) a reconstructor \mathcal{R} that lifts these coefficients back to the function space by expanding them in the learned basis.

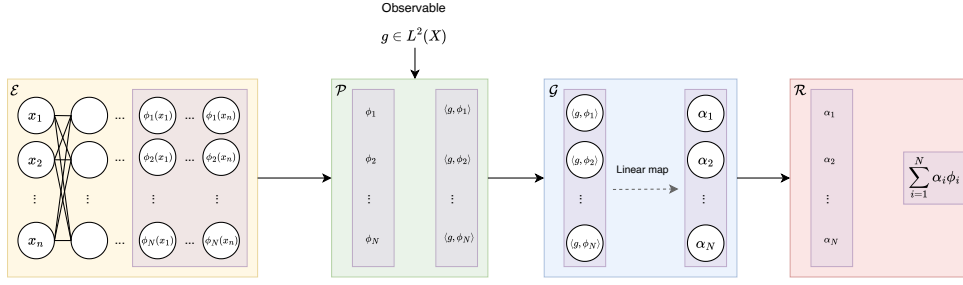


Fig. 1: SABON consists of an encoder \mathcal{E} , a latent projection \mathcal{P} , a linear map \mathcal{G} , and a reconstruction map \mathcal{R} . The encoder learns basis functions $\{\phi_j\}_{j=1}^N$, while $\mathcal{G}: \mathbb{R}^N \rightarrow \mathbb{R}^N$ approximates the action of \mathcal{L} on $V = \text{span}\{\phi_j\}_{j=1}^N$. The reconstruction map recovers a function from its coefficients in the latent space.

Two inputs are needed for the above architecture: the discretization $\{x_i\}_{i=1,\dots,n} \subset X$ where all maps are evaluated, and the observable function g , represented by its evaluation over these sampling points $[g(x_1), g(x_2), \dots, g(x_n)]^\top$.

We explain the SABON components in turn.

Encoder (\mathcal{E}). The encoder in SABON is a stack of vector-valued neural networks, each applied pointwise to one grid element. Recall from (2.1) that $\hat{\phi}: \mathbb{R}^d \rightarrow \mathbb{R}^N$ is the vector-valued network defined in the embedding of X in \mathbb{R}^d . Then the encoder

$$\mathcal{E}: (\mathbb{R}^d)^n \rightarrow (\mathbb{R}^N)^n \cong \mathbb{R}^{Nn}, \quad \mathcal{E}((x_1, \dots, x_n)) = (\hat{\phi}(x_1), \dots, \hat{\phi}(x_n))$$

acts by evaluating $\hat{\phi}$ at every grid point. Written componentwise, the output is the column-major vector

$$[\phi_1(x_1), \dots, \phi_N(x_1), \phi_1(x_2), \dots, \phi_N(x_2), \dots, \phi_1(x_n), \dots, \phi_N(x_n)]^\top \in \mathbb{R}^{Nn}.$$

The collection $\{\phi_j\}_{j=1}^N$ forms the learned neural basis of the subspace V introduced above.

Projection (\mathcal{P}). The projection block computes¹ $\{\langle g, \phi_j \rangle\}_{j=1,\dots,N}$ for an observable $g \in L^2(X)$ and a set of learned basis functions $\{\phi_j\}_{j=1}^N$. In more general terms, we define $\mathcal{P}_{\{\phi_j\}_{j=1}^N}: L^2(X) \rightarrow \mathbb{R}^N$ via

$$(2.2) \quad \mathcal{P}_{\{\phi_j\}_{j=1}^N}(g) = (\langle g, \phi_1 \rangle, \dots, \langle g, \phi_N \rangle)$$

We shall sometimes omit the subscript of \mathcal{P} .

Map \mathcal{G} in latent space. The action of the transfer/Koopman operator is represented by a linear map implemented in block \mathcal{G} . The coefficients $\langle g, \phi_j \rangle$, $j = 1, \dots, N$ in the latent space are fed into \mathcal{G} , which learns the action of $\hat{\mathcal{L}}$ in the latent space. That is, the block \mathcal{G} consists of a learnable linear map capable of transforming the coefficients of g when represented in the basis $\{\phi_j\}_{j=1}^N$ into the corresponding coefficients of $\hat{\mathcal{L}}(g)$ in the same basis.

¹in practice, this inner product is evaluated as $\frac{1}{n} \sum_{i=1}^n g(x_i) \phi_j(x_i)$.

Reconstruction (\mathcal{R}). The architecture employs a reconstruction block that converts the latent coefficients produced by the linear map \mathcal{G} into the approximation of the transformed observable

$$\hat{\mathcal{L}}(g)(x) = \sum_{j=1}^N \alpha_j \phi_j(x).$$

Because the same functional expression can reconstruct any element of the span of the learned basis, we keep the generic definition of $\mathcal{R}_{\{\phi_j\}_{j=1}^N} : \mathbb{R}^N \rightarrow L^2(X)$ as

$$(2.3) \quad \mathcal{R}_{\{\phi_j\}_{j=1}^N}(a_1, \dots, a_N) = \sum_{j=1}^N a_j \phi_j.$$

To simplify the notation, we will also sometimes omit the subscript in the sequel. The coefficients serving as input to \mathcal{R} will always be clear from the context (i.e. which maps are composed with \mathcal{R}).

One of the key features of SABON is that it simultaneously optimises the learned subspace and the operator action. This is performed through a suitable loss function comprised of two components (in practice these are calculated with their discrete counterparts using evaluations at the sample points $\{x_i\}_{i=1}^n$):

1. The composition $\mathcal{R} \circ \mathcal{G} \circ \mathcal{P}$, which approximates the projected action of \mathcal{L} on V , has the loss term:

$$(2.4) \quad \mathcal{E}_1(\mathcal{L}, \mathcal{G}, \mathcal{P}, \mathcal{R}, g) := \frac{\|\mathcal{L}(g) - \mathcal{R} \circ \mathcal{G} \circ \mathcal{P}(g)\|_2}{\|\mathcal{L}(g)\|_2}.$$

2. A sparsity penalty encourages the learned basis functions to have local support:

$$(2.5) \quad \mathcal{E}_2(\{\phi_j\}_{j=1}^N) = \frac{1}{N} \sum_{j=1}^N \|\phi_j\|_{L^1}.$$

The complete loss function is

$$(2.6) \quad J(\mathcal{L}, \mathcal{G}, \mathcal{P}, \mathcal{R}, g, \{\phi_j\}_{j=1}^N) = \beta_1 \mathcal{E}_1(\mathcal{L}, \mathcal{G}, \mathcal{P}, \mathcal{R}, g) + \beta_2 \mathcal{E}_2(\{\phi_j\}_{j=1}^N),$$

where $\beta_1, \beta_2 \geq 0$.

We also explored supplementary projection penalties aimed at reconstructing observables after their projection onto the subspace. The first variant penalised deviations in reconstructing the original observable:

$$\mathcal{E}_{p_1}(\mathcal{P}, \mathcal{R}, g) := \frac{\|\text{Id}(g) - \mathcal{R} \circ \mathcal{P}(g)\|_2}{\|\text{Id}(g)\|_2},$$

while the second variant addressed the reconstruction of $\mathcal{L}(g)$ after projection onto the learned subspace:

$$\mathcal{E}_{p_2}(\mathcal{P}, \mathcal{R}, \mathcal{L}, g) := \frac{\|\text{Id}(\mathcal{L}(g)) - \mathcal{R} \circ \mathcal{P}(\mathcal{L}(g))\|_2}{\|\text{Id}(g)\|_2}$$

where Id is the identity operator on $L^2(X)$. In practice, we found that the first penalty sometimes adversely affected the invariance property central to our goals — eigenpair reconstruction and subspace invariance. Conversely, the second penalty demonstrated a neutral impact, presumably due to its redundancy with \mathcal{E}_1 , since effective operator approximation implicitly requires accurate reconstruction after projection.

Finally, we discuss the activation functions employed in the proposed architecture. For the \mathcal{G} network, which is learning the action of a linear operator (transfer or Koopman), we selected a linear activation function, namely the identity function, and set the bias term to zero. The activation functions for the encoder block (\mathcal{E}) can be chosen among the usual candidates, and we had the best results with ReLU in our experiments.

The combined architecture and loss in SABON are structured so that the learned basis $\{\phi_j\}_{j=1}^N$ (i) is approximately orthogonal, (ii) spans a subspace V that is very close to invariant under the Perron–Frobenius/Koopman operator, and (iii) has a tendency toward local support, guided by the sparsity term \mathcal{E}_2 in the loss function.

Further, \mathcal{E}_1 *simultaneously optimises* for a good finite-dimensional approximation of the operator action and enforces that $\{\phi_j\}_{j=1}^N$ spans a space V well suited for representing $\mathcal{L}(g)$. A final rescaling step yields an orthonormal basis.

2.2. Universal approximation theorem. Hua *et al.* (2023) [16] consider a general, possibly nonlinear, operator \mathcal{J} between two distinct Hilbert spaces.

$$\mathcal{J}: \mathcal{H}_{\text{in}} \longrightarrow \mathcal{H}_{\text{out}}, \quad \mathcal{H}_{\text{in}} \neq \mathcal{H}_{\text{out}}$$

and therefore employ two autoencoders to learn separate finite-dimensional subspaces for the domain and codomain.

In this work, we restrict ourselves to the transfer and Koopman operators \mathcal{L} associated with a dynamical system. Each of these operators map $L^2(X)$ into $L^2(X)$, so only a single subspace $V \subset L^2(X)$ is required to approximate both the observable g and its image $\mathcal{L}(g)$. Consequently, in contrast to [16], one should instead use a *single* encoder. We state an approximation theorem in this alternate setting.

THEOREM 2.1. *Let $X \subset \mathbb{R}^d$ be compact and let $T : X \rightarrow X$ be the evolution dynamics on X . Let $\mathcal{L} : L^2(X) \rightarrow L^2(X)$ be continuous and denote either the Koopman or the transfer operator associated with T . Given $N \in \mathbb{N}$ and a family $\phi = (\phi_1, \dots, \phi_N) \subset L^2(X)$ define*

$$\begin{aligned} \mathcal{P}_\phi : L^2(X) &\rightarrow \mathbb{R}^N, & \mathcal{P}_\phi(g) &= (\langle g, \phi_1 \rangle, \dots, \langle g, \phi_N \rangle)^\top, \\ \mathcal{R}_\phi : \mathbb{R}^N &\rightarrow L^2(X), & \mathcal{R}_\phi(a_1, \dots, a_N) &= \sum_{j=1}^N a_j \phi_j. \end{aligned}$$

Then for each compact set $K \subset L^2(X)$ and any $0 < \epsilon < 1$ there exist $N > 0$, a neural basis $\phi = (\phi_1, \phi_2, \dots, \phi_N) : X \rightarrow \mathbb{R}^N$ and a linear map $\mathcal{G} : \mathbb{R}^N \rightarrow \mathbb{R}^N$ such that the

operator $\hat{\mathcal{L}} := \mathcal{R}_\phi \circ \mathcal{G} \circ \mathcal{P}_\phi$ satisfies

$$\sup_{g \in \mathcal{K}} \left\| \mathcal{L}(g) - \hat{\mathcal{L}}(g) \right\|_{L^2(X)} \leq \epsilon.$$

Remark 2.2. Examples of compact sets $\mathcal{K} \in L^2(X)$ with $X \subset \mathbb{R}^d$, include (i) the closed unit ball of any finite-dimensional subspace in $L^2(X)$ and (ii) the closed unit ball of $H^1(X)$, for $d \geq 2$ and X a bounded C^1 domain (its boundary is locally a C^1 graph). The latter is compact in $L^2(X)$ by the Rellich–Kondrachov Embedding Theorem (e.g. Theorem 9.16 [6]).

Two convenient sufficient conditions that guarantee the continuity of \mathcal{L} are:

1. T is measurable and μ –invariant, so that \mathcal{L} acts as an isometry on $L^2(X)$. The circle rotation in subsection 3.3 is a representative example with $\mu = \text{Lebesgue}$;
2. T is non-singular with respect to μ and there exists a constant $c > 0$ such that

$$0 < c^{-1} \leq \frac{d(\mu \circ T^{-1})}{d\mu} \leq c < \infty$$

μ almost everywhere. The Anosov map in subsection 3.4 is a representative example with $\mu = \text{Lebesgue}$.

Proof of Theorem 2.1. The proof proceeds almost exactly as in [16, Theorem 2.2], so we omit the repeated details and focus on the necessary modifications. We need only one neural basis $\{\phi_1, \dots, \phi_N\} \subset L^2(X)$ for both the input and output spaces. The universal approximation property [16, Theorem 2.1] ensures we can approximate each $g \in \mathcal{K}$ by an element $g^N \in \text{span}\{\phi_j\}_{j=1}^N$. Let $\mathcal{K}_\mathcal{L} := \mathcal{K} \cup \mathcal{L}(\mathcal{K})$ and choose N and ϕ by [16, Theorem 2.1] so that, writing $Q := \mathcal{R}_\phi \mathcal{P}_\phi$,

$$\sup_{v \in \mathcal{K}_\mathcal{L}} \|v - Qv\|_{L^2(X)} \leq \eta \quad \text{for some } \eta > 0.$$

Next, since Q is continuous and \mathcal{K} is compact, $\mathcal{K}_{Q\mathcal{L}} := \mathcal{K}_\mathcal{L} \cup Q(\mathcal{K}_\mathcal{L})$ is compact, hence \mathcal{L} is uniformly continuous on $\mathcal{K}_{Q\mathcal{L}}$ with modulus of continuity $\omega_\mathcal{L}$.

The main difference appears in the error decomposition. In [16], one bounds three terms to handle potentially different neural bases for input and output spaces, but here we merge everything into two terms. If $\hat{\mathcal{L}} := \mathcal{R}_{\{\phi_j\}_{j=1}^N} \circ \mathcal{G} \circ \mathcal{P}_{\{\phi_j\}_{j=1}^N}$, then for $g \in \mathcal{K}$

$$\begin{aligned} \|\mathcal{L}(g) - \hat{\mathcal{L}}(g)\|_{L^2(X)} &\leq \left\| \mathcal{L}(g) - \mathcal{R}_{\{\phi_j\}_{j=1}^N} \circ \mathcal{P}_{\{\phi_j\}_{j=1}^N} \circ \mathcal{L}(g) \right\|_{L^2(X)} \\ &\quad + \left\| \mathcal{R}_{\{\phi_j\}_{j=1}^N} \circ \mathcal{P}_{\{\phi_j\}_{j=1}^N} \circ \mathcal{L}(g) - \mathcal{R}_{\{\phi_j\}_{j=1}^N} \circ \mathcal{G} \circ \mathcal{P}_{\{\phi_j\}_{j=1}^N}(g) \right\|_{L^2(X)}. \end{aligned}$$

For the first term, since $\mathcal{L}(g) \in \mathcal{L}(\mathcal{K}) \subset \mathcal{K}_\mathcal{L}$, we have $\|\mathcal{L}(g) - Q\mathcal{L}(g)\| \leq \eta$. Setting $\mathcal{G} := \mathcal{P}_\phi \circ \mathcal{L} \circ \mathcal{R}_\phi$ in the second term we obtain

$$\|Q\mathcal{L}(g) - Q\mathcal{L}(Qg)\| \leq \|Q\| \|\mathcal{L}(g) - \mathcal{L}(Qg)\| \leq \|Q\| \omega_\mathcal{L}(\|g - Qg\|) \leq \|Q\| \omega_\mathcal{L}(\eta).$$

Everything else remains unchanged from [16, Theorem 2.2], and thus we conclude

$$\sup_{g \in \mathcal{K}} \|\mathcal{L}(g) - \hat{\mathcal{L}}(g)\|_{L^2(X)} \leq \eta + \|Q\| \omega_\mathcal{L}(\eta).$$

Choosing N and ϕ so that the right-hand side is smaller than ϵ yields the claim. \square

3. Numerical examples. In this section, we illustrate the results obtained with our architecture through two representative examples. We consider the Perron–Frobenius operator in both examples, but the procedure is identical for training data generated by the Koopman operator. The first example considers a circle rotation, highlighting the recovery of spectral properties of the associated linear operator. The second example examines a nonlinearly perturbed version of Arnold’s cat map on the two-torus. This nonlinear map is highly anisotropic in state space and the eigenfunctions of the transfer operator are known to be *distributions* rather than functions [15, 9]. Through this very challenging example, we demonstrate how the learned basis functions can nevertheless successfully adapt to the system dynamics to construct an almost perfectly invariant subspace V .

3.1. Data generation. Both examples in this paper — the circle rotation and the perturbed cat map — are dynamical systems on periodic domains. We therefore require periodic observables, and we use random trigonometric polynomials to provide a rich class of training functions. To train the proposed architecture, we consider the intrinsic dimension $d' = \dim X$ and generate a dataset of D random trigonometric polynomial functions defined on a d' -dimensional domain. Each such function is constructed as a finite linear combination of sinusoidal basis functions (sine and cosine terms) in each dimension, with randomly chosen coefficients. Formally, a general d' -dimensional trigonometric polynomial of maximum order K can be written as a linear combination of terms of the form $\prod_{j=1}^{d'} \Psi_j(k_j x_j)$, where each $\Psi_j(\cdot)$ is either $\sin(\cdot)$ or $\cos(\cdot)$, and each integer frequency k_j ranges from 1 to K for $\sin(\cdot)$ and from 0 to K for $\cos(\cdot)$. In other words, no oscillatory component in any dimension exceeds frequency K . The coefficients in the linear combination are real numbers drawn at random uniformly in $[-1, 1]$. Note that the inclusion of $k_j = 0$ allows constant (zero-frequency) components in each dimension as well. For example, in $d' = 2$ dimensions (with coordinates x_1 and x_2), such trigonometric polynomials take the form:

$$\begin{aligned} f(x_1, x_2) = & c_1 \sin(k_1 x_1) \sin(k_2 x_2) + c_2 \sin(k_1 x_1) \cos(k_2 x_2) \\ & + c_3 \cos(k_1 x_1) \sin(k_2 x_2) + c_4 \cos(k_1 x_1) \cos(k_2 x_2), \end{aligned}$$

with $k_1, k_2 \in \{1, \dots, K\}$ for the sine terms and $k_1, k_2 \in \{0, 1, \dots, K\}$ for the cosine terms. In the general d' -dimensional case, each term is a product of trigonometric functions, one for each of the d' coordinates, with frequencies up to K in each coordinate. Such functions contain a rich variety of mixed-frequency components across all dimensions.

Once the D random functions f_j are generated as described above, we apply \mathcal{L} to each of them to obtain the corresponding output functions $\mathcal{L}f_j$. This yields a training set of D input-output pairs $\{f_j; \mathcal{L}f_j\}_{j=1}^D$. In our training, $[f_j(x_1), f_j(x_2), \dots, f_j(x_n)]^\top$ serves as an input function sampled on the discretization $\{x_i\}_{i=1, \dots, n}$, and $[\mathcal{L}f_j(x_1), \mathcal{L}f_j(x_2), \dots, \mathcal{L}f_j(x_n)]^\top$ is treated as the target output. By using trigonometric polynomials as input functions, we ensure that the action of \mathcal{L} is well defined and smooth on these inputs. This property simplifies the generation of training data when $\mathcal{L}f_j$ can be computed analytically, and preserves the continuity that is important for machine-learned approximations.

In summary, our choice of trigonometric polynomials is natural because (i) they form a very expressive class of functions, which are dense in the space of continuous and square-integrable periodic functions, (ii) they are smooth, facilitating stable

training of the network (gradients can be computed reliably, and there are no discontinuities or singularities in the input data), and (iii) their generation is straightforward and computationally inexpensive.

3.2. Examples setup. We train on collections of functions as described in subsection 3.1. The validation and test sets are drawn from the same underlying class of functions as our training data. The parameters of each dataset are summarized in Table 1.

Table 1: Data parameters for the circle rotation and perturbed cat map. We list the number of training functions (D), maximum trigonometric polynomial order (K), number of validation functions, number of test functions, and the grid size (n).

Example	D	K	Validation	Test	n
Circle rotation	1000	9	500	100	100
Perturbed cat map	3000	5	500	500	10000

The training set is used to fit the model parameters by minimising the defined loss. During training, we periodically evaluate the current model on the validation set. We also explore alternative hyperparameter settings — e.g. learning rate, network depth, and regularisation strength—and retain the configuration that achieves the lowest validation error. Only after all training and hyperparameter selection are complete do we assess the model on the test set. This provides an unbiased estimate of the model’s performance on unseen functions, since the test data is not used to guide model selection.

For more complex dynamics, like the nonlinearly perturbed cat map, we employ larger architectures to capture the increased complexity. The specifics of each architecture, including the dimensions, activation functions, and the number of learned basis functions are shown in Table 2.

Table 2: Architecture specifics for the circle rotation and perturbed cat map. We list the encoder (\mathcal{E}) and approximation networks (\mathcal{G}), their hidden layer architectures (e.g. 5×512 denotes five hidden layers with 512 units each), and activation functions. The dashes indicate that there are no hidden layers for the network \mathcal{G} since it is learning a linear map in \mathbb{R}^N .

Example	Encoder (\mathcal{E})		Approximation (\mathcal{G})		N
	Hidden layers	Activ.	Hidden layers	Activ.	
Circle rotation	5×512	ReLU	-	Identity	19
Perturbed cat map	5×2048	ReLU	-	Identity	225

3.3. Transfer operator for a circle rotation. The circle rotation map $T : S^1 \rightarrow S^1$ is a transformation in the circle given by $T(\theta) = \theta + \alpha \pmod{2\pi}$. For our numerical examples, we choose $\alpha = -1$. To avoid discontinuities at the endpoints of the domain interval, we embed the unit-radius circle S^1 into \mathbb{R}^2 , identifying each θ with $(\cos \theta, \sin \theta) \in \mathbb{R}^2$. Thus the ambient dimension is $d = 2$ while the intrinsic dimension remains $d' = 1$.

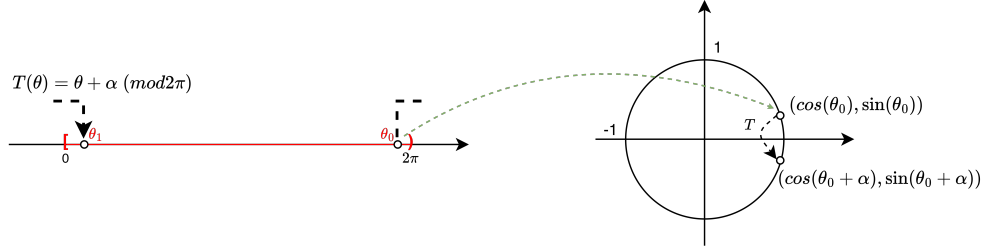


Fig. 2: Embedding of the circle-rotation map $T(\theta) = \theta + \alpha \pmod{2\pi}$ from the interval $[0, 2\pi)$ into the unit circle $S^1 \subset \mathbb{R}^2$. Each angle θ is sent to its Cartesian coordinates $(\cos \theta, \sin \theta)$, removing the discontinuity that would occur at $\theta = 0 \equiv 2\pi$ in the interval picture. The initial point θ_0 is chosen close to the right-hand endpoint of the interval to highlight the jump that is resolved by the embedding.

After the learning routine, we obtain both a set of basis functions spanning a subspace invariant under the transfer operator and an estimator for its action. Figure 3 displays how the learned estimator performs on unseen data for various sparsity scenarios.

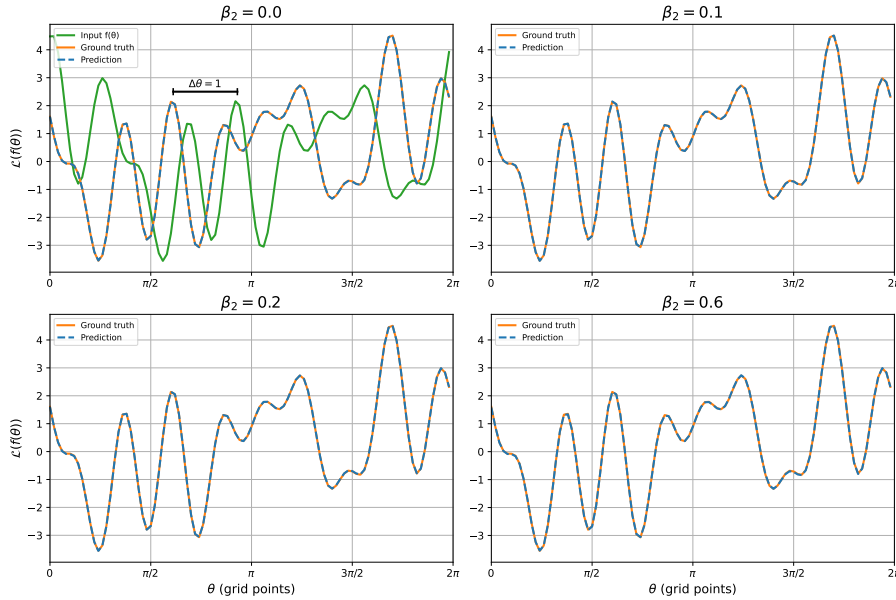


Fig. 3: Performance of the learned operator approximation on unseen input data, for different levels of sparsity. No appreciable difference in performance is seen across the various sparsity penalties.

The corresponding quantitative results — mean relative L^2 errors averaged over the test set — are summarised in Table 3. Table 3 is consistent with Figure 3; there is little change in relative error observed with increasing sparsity.

Table 3: Mean relative L^2 error of each model on the test set.

Model	Mean relative error
No Sparsity ($\beta_2 = 0$)	3.974×10^{-3}
Sparsity ($\beta_2 = 0.1$)	3.641×10^{-3}
Sparsity ($\beta_2 = 0.2$)	3.958×10^{-3}
Sparsity ($\beta_2 = 0.6$)	6.234×10^{-3}

The approximately invariant subspace is spanned by the set of basis functions depicted in Figure 4. By introducing a sparsity penalty, these functions gain increasingly localised support, as shown in Figure 4.

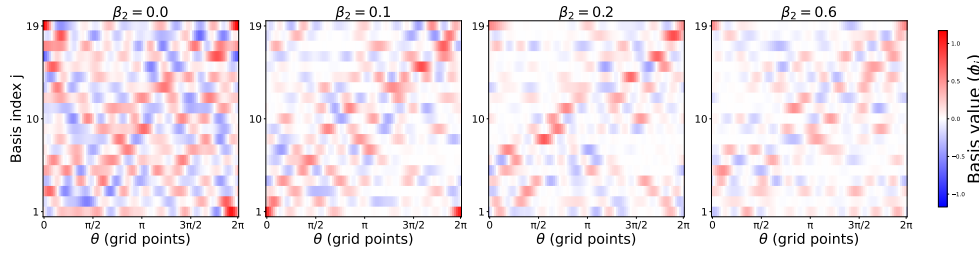


Fig. 4: Basis functions obtained under different sparsity penalties: each panel displays a distinct basis for a distinct sparsity penalty. In a single panel, the state space coordinates (the angles $\theta \in S^1$) are along the x -axis, and each row shows the values of a different basis function. Higher sparsity encourages localisation, which is reflected in more concentrated regions of support.

After L^2 -normalising the learned basis, we examine the Gram matrix, defined as

$$(3.1) \quad M_{kj} = \langle \phi_k, \phi_j \rangle, \quad k, j = 1, \dots, N,$$

in Figure 5. The introduction of a sparsity penalty slightly improves orthogonality.

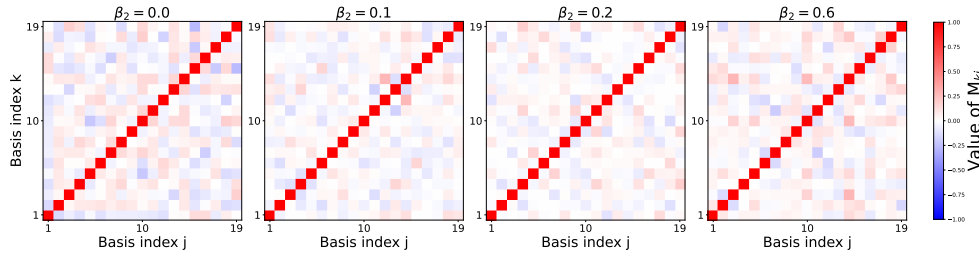


Fig. 5: Gram matrix of the filtered and normalised basis functions

We now recover the spectral properties of \mathcal{L} from the learned estimator $\hat{\mathcal{L}}$. Consider the collection of learned basis functions $\{\phi_j\}_{j=1}^N \subset L^2(X)$. Suppose an observ-

able $g \in L^2(X)$ can be represented as

$$g = \sum_{j=1}^N \beta_j \phi_j,$$

where $\beta = (\beta_1, \dots, \beta_N)^T \in \mathbb{R}^N$ is the coefficient vector.

Applying the projection operator \mathcal{P}_ϕ to g yields

$$\mathcal{P}_\phi(g) = \begin{pmatrix} \langle g, \phi_1 \rangle \\ \vdots \\ \langle g, \phi_N \rangle \end{pmatrix} = \begin{pmatrix} \langle \sum_{j=1}^N \beta_j \phi_j, \phi_1 \rangle \\ \vdots \\ \langle \sum_{j=1}^N \beta_j \phi_j, \phi_N \rangle \end{pmatrix} = M\beta,$$

where M is the Gram matrix as defined in (3.1).

The learned operator is composed as $\hat{\mathcal{L}} = \mathcal{R}_\phi \circ \mathcal{G} \circ \mathcal{P}_\phi$ where \mathcal{G} is an $N \times N$ matrix representing the dynamics in coefficient space. When $\hat{\mathcal{L}}$ is applied to g we obtain the following linear transformation:

$$\hat{\mathcal{L}}g = \mathcal{R}_\phi(\mathcal{G}(\mathcal{P}_\phi(g))) = \mathcal{R}_\phi(\mathcal{G}(M\beta)) = \sum_{j=1}^N (\mathcal{G}M\beta)_j \phi_j.$$

A function g with coefficient vector β is an eigenfunction of $\hat{\mathcal{L}}$ with eigenvalue λ if and only if $\hat{\mathcal{L}}g = \lambda g$. This means

$$\sum_{j=1}^N (\mathcal{G}M\beta)_j \phi_j = \lambda \sum_{j=1}^N \beta_j \phi_j.$$

Since the basis functions are approximately linearly independent, we must have

$$(3.2) \quad \mathcal{G}M\beta = \lambda\beta.$$

Equation (3.2) is a generalised eigenvalue problem of size $N \times N$. Solving it yields eigenvalue-eigenvector pairs $(\lambda_k, \beta^{(k)})$ for $k = 1, \dots, N$. The corresponding eigenfunctions are

$$g_k = \sum_{j=1}^N \beta_j^{(k)} \phi_j, \quad k = 1, \dots, N.$$

For the circle rotation, one can derive the eigenpairs analytically. The transfer operator for the circle rotation is

$$(\mathcal{L}g)(\theta) = g(\theta - \alpha).$$

Using the eigenfunction ansatz $\psi_k(\theta) = e^{ik\theta}$ for $k \in \mathbb{Z}$, we have

$$(\mathcal{L}\psi_k)(\theta) = e^{ik(\theta - \alpha)} = e^{-ik\alpha} \psi_k(\theta) \implies \lambda_k = e^{-ik\alpha}, \quad \psi_k(\theta) = e^{ik\theta},$$

which shows that we have eigenpairs (λ_k, ψ_k) , $k \in \mathbb{Z}$. Thus, the leading eigenvalues take the form

$$\lambda_{\pm 1} = e^{\pm i\alpha}.$$

These analytic expressions match well with our numerical experiments, which were performed with the model parameter $\beta_2 = 0.6$; see Figure 6. Furthermore, the leading learned eigenfunctions coincide perfectly with the leading analytic eigenfunctions; see Figure 7.

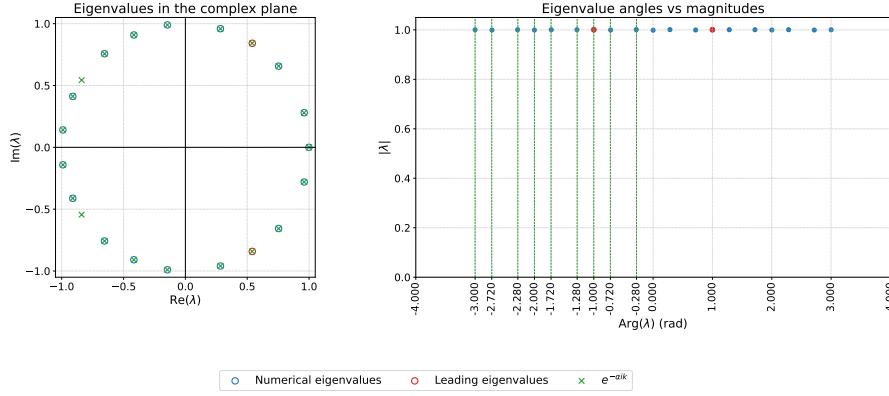


Fig. 6: **Left:** Eigenvalues of the Perron–Frobenius operator for a circle rotation by $\alpha = -1$ radians. Numerical eigenvalues (blue circles; leading pair corresponding to $k = \pm 1$ shown as red circles) coincide with the analytic spectrum (green crosses) **Right:** Magnitude versus argument of the same eigenvalues. The dashed green vertical lines mark angles that are positive integer multiples of α , underscoring that the additional numerical eigenvalues are dynamically meaningful, but duplicate information from the lowest-order eigenvalues.

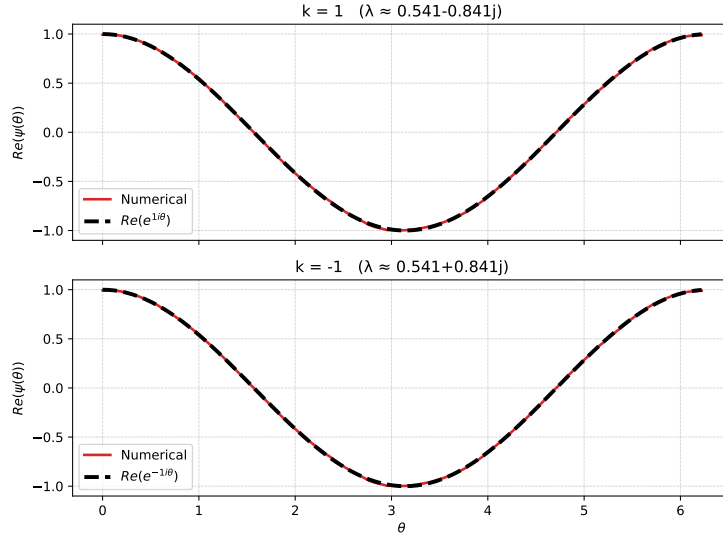


Fig. 7: Real parts of the leading eigenfunctions of the transfer operator. The analytic eigenfunction is plotted in dashed black, while its numerical counterpart is in solid red. In both cases the numerical eigenfunctions coincide with the analytic curves.

Finally, we demonstrate the invariance of the learned subspace under the Perron–Frobenius operator. On the grid $\{x_i\}_{i=1,\dots,n}$ define

$$\Phi = [\phi_j(x_i)]_{i=1,\dots,n; j=1,\dots,N} \in \mathbb{R}^{n \times N}, \quad \Psi = [\mathcal{L}(\phi_j)(x_i)]_{i=1,\dots,n; j=1,\dots,N} \in \mathbb{R}^{n \times N},$$

and set $r = \text{rank } \Phi = \text{rank } \Psi \leq N$. We wish to determine how close the r -dimensional column space of Φ is to the r -dimensional column space of Ψ , and we do this by computing principal angles between these two subspaces. Following [14, Algorithm 6.4.3] we form the QR decomposition

$$\Phi = Q_\Phi R_\Phi, \quad \Psi = Q_\Psi R_\Psi,$$

with orthogonal $Q_\Phi, Q_\Psi \in \mathbb{R}^{n \times n}$ and upper-triangular $R_\Phi, R_\Psi \in \mathbb{R}^{n \times N}$. Denote by $Q_\Phi^{(r)}$ and $Q_\Psi^{(r)}$ the first r columns of Q_Φ and Q_Ψ . If $0 \leq \theta_1 \leq \dots \leq \theta_r$ are the principal angles between the subspaces spanned by Φ and Ψ , then

$$\cos \theta_k = \sigma_k[(Q_\Phi^{(r)})^\top Q_\Psi^{(r)}], \quad k = 1, \dots, r,$$

To avoid numerical issues associated with the classical cosine-based computation for small angles and the sine-based approach for angles near $\frac{\pi}{2}$, we employed the combined technique [20] that uses the cosine-based method initially and switches to the sine-based approach for principal angles smaller than $\frac{\pi}{4}$. Note that the computation of principal angles is extremely sensitive to numerical precision. Therefore, we use higher precision floating-point arithmetic for these operations in both of our examples to ensure accurate results.

From these angles $\theta = (\theta_1, \dots, \theta_N)$, we report three standard subspace-distance metrics:

1. the geodesic distance $d_{\max} = \max_k \theta_k$,
2. the chordal distance $d_{\text{ch}} = \|\sin \theta\|_2$,
3. the projection distance $d_{\text{pr}} = \sin d_{\max}$.

Table 4: Subspace-distance measures between $\text{span}\{\phi_j\}_{j=1}^N$ and $\text{span}\{\mathcal{L}(\phi_j)\}_{j=1}^N$

Metric	$\beta_2 = 0$	$\beta_2 = 0.1$	$\beta_2 = 0.2$	$\beta_2 = 0.6$
Geodesic (d_{\max})	3.983×10^{-2}	3.621×10^{-2}	3.869×10^{-2}	4.008×10^{-2}
Chordal (d_{ch})	3.982×10^{-2}	3.621×10^{-2}	3.868×10^{-2}	4.008×10^{-2}
Projection (d_{pr})	1.760×10^{-2}	1.906×10^{-2}	2.146×10^{-2}	1.732×10^{-2}

Smaller values of the principal angles θ_k indicate that the two subspaces are closer, and hence the learned subspace approaches invariance under \mathcal{L} . Across all sparsity levels β_2 , the reported distances remain on the order of 10^{-2} , providing strong evidence of a learned subspace that is nearly invariant under the true operator \mathcal{L} .

We close this example by discussing the choice of $N = 19$ basis functions. Recall we trained $\hat{\mathcal{L}}$ using trigonometric polynomials up to order 9 (equivalently linear combinations of real Fourier modes up to order 9). As discussed above, each two-dimensional real subspace spanned by $\theta \mapsto \sin(k\theta)$ and $\theta \mapsto \cos(k\theta)$ is an eigenspace with eigenpair $\lambda_{\pm k}$. Thus, in this special situation of circle rotation dynamics, the input and output data lie in the same 19-dimensional ($19 = 2 \times 9 + 1$) subspace. Increasing the learned basis cardinality N beyond 19 will not impact the prediction error, but the

principal angles beyond the first 19 will increase because these additional dimensions will effectively be unable to be controlled with 9th-order input/output data.

3.4. Transfer operator for a nonlinearly perturbed Arnold’s cat map.

We consider a nonlinear perturbation of the (linear and hyperbolic) Arnold’s cat map of the two-torus $X = \mathbb{T}^2$ introduced in [9]:

$$T : \mathbb{T}^2 \rightarrow \mathbb{T}^2, \quad T(x, y) = (2x + y + 2\delta \cos(2\pi x), x + y + \delta \sin(4\pi y + 1)) \pmod{1},$$

with $\delta = 0.01$. With this perturbation, T remains Anosov and therefore has an SRB measure μ [5, Theorem 4.12]. The spectral theory for Anosov diffeomorphisms is challenging and relies on carefully constructed anisotropic Banach spaces (e.g. [15]) that are adapted to the unstable and stable foliations. In this example, we let $\mathcal{L}f = f \circ T^{-1} / |\det DT \circ T^{-1}|$ be the Perron–Frobenius operator, and consider $\mathcal{L} : L^2(X, m) \rightarrow L^2(X, m)$ where m is Lebesgue measure on the flat torus. Note the additional determinant term in the definition of \mathcal{L} ; the constant function is no longer the leading eigenfunction of \mathcal{L} . In fact, the object μ satisfying $\mathcal{L}\mu = \mu$ is in general a *distribution* and need not lie in $L^2(\mathbb{T}^2, m)$. The fixed distribution μ may be identified with the SRB measure and describes the long-term distribution of infinitely long trajectories of T for *Lebesgue almost all* initial conditions $x \in \mathbb{T}^2$. This distribution of infinitely long trajectories is accessible through the fixed point of \mathcal{L} ; this is one of the many advantages of studying transfer operators.

To eliminate the discontinuities that arise at the edges of the unit square, we embed \mathbb{T}^2 into \mathbb{R}^4 by mapping each (x, y) to its pair of complex phases $(\cos 2\pi x, \sin 2\pi x, \cos 2\pi y, \sin 2\pi y)$. That is, we treat a problem with intrinsic dimension $d' = 2$ in a higher ambient space with dimension $d = 4$. We first evaluate our model’s ability to approximate the Perron–Frobenius operator on an unseen observable. To highlight the anisotropic nature of the learned basis everywhere in the phase space, we chose not to apply the sparsity penalty throughout this example. Figure 8 displays an unseen input observable g , the ground-truth image, and our network’s prediction. The accuracy is quantified by the relative L^2 error of 1.225×10^{-2} on the full test set.

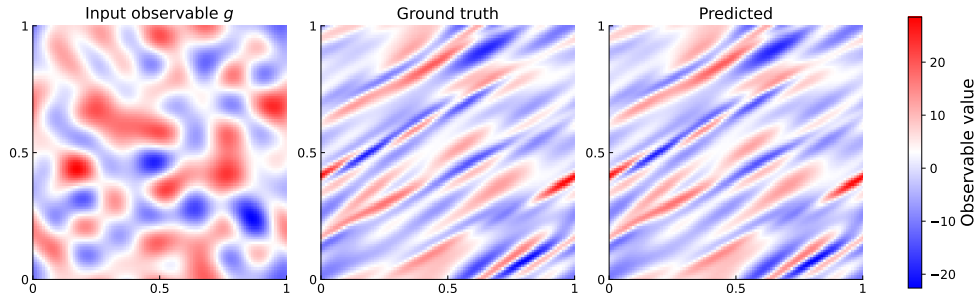


Fig. 8: Input and output for the Perron–Frobenius operator of a perturbed Arnold’s cat map. Left to right, the three panels show (i) an unseen input observable g , (ii) the corresponding ground-truth output from the true transfer operator, (iii) and the corresponding predicted output from our learned transfer operator. The mean L^2 relative error over the full test set is 1.225×10^{-2} .

Next, we analyse the learned set of basis functions $\{\phi_j\}_{j=1}^N$ that span the invariant subspace V . Figure 9 shows representative basis functions obtained without sparsity

penalty. The basis functions obtained through the proposed network show unmistakable alignment with contracting and expanding directions of the nonlinear dynamics generated by T .

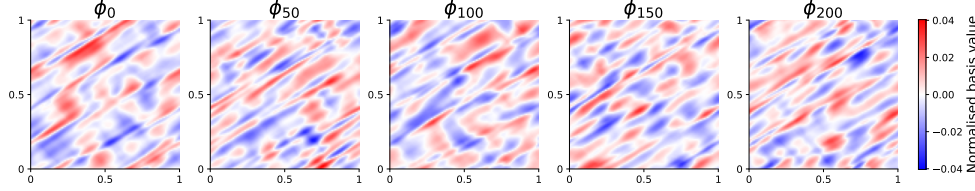


Fig. 9: Representative basis functions learned by the network. The patterns exhibit structures that align with the map’s contracting and expanding directions, illustrating how the learned invariant subspace is adapted to the underlying dynamics.

The Gram matrix of the L^2 -normalised learned basis functions defined in (3.1) is illustrated in Figure 10. Its nearly diagonal form shows that our training scheme implicitly promotes approximate orthogonality, even without an explicit sparsity term.

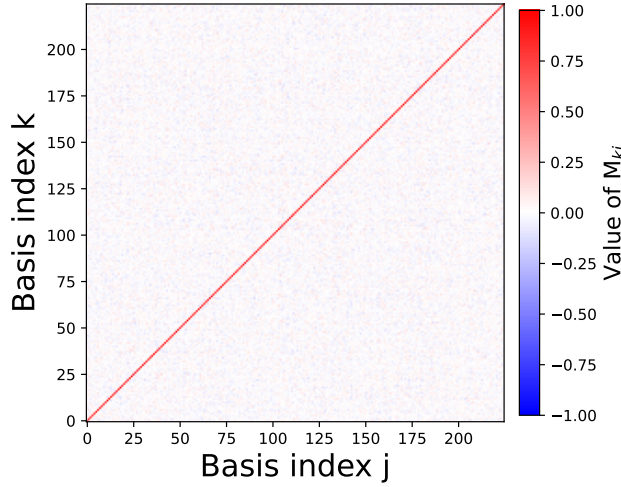


Fig. 10: Gram matrix of the learned basis functions (after L^2 normalisation). The diagonal structure shows that the network has produced a nearly orthogonal collection, despite the absence of an explicit sparsity constraint.

We now examine the spectral properties of the learned Perron–Frobenius approximator. Figure 11 displays the eigenvalues; the leading eigenvalue at $\lambda = 1$ confirms the presence of an invariant measure as a fixed point of the Perron–Frobenius operator.

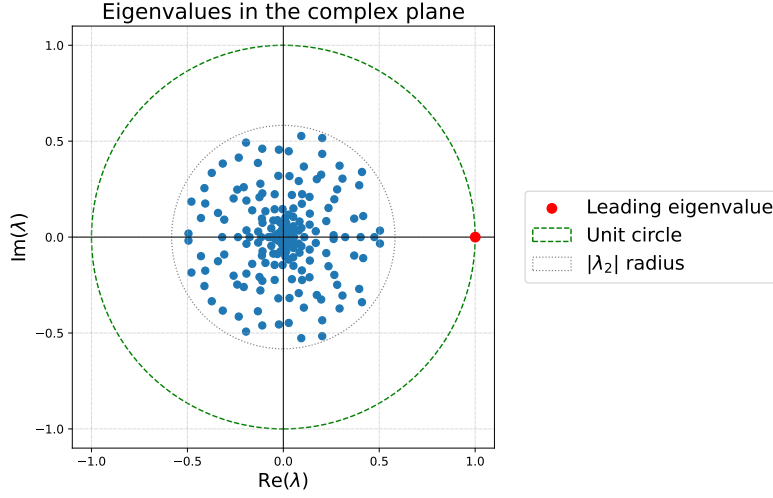


Fig. 11: Eigenvalues of the learned Perron–Frobenius operator for the model with no sparsity penalty. The leading eigenvalue (corresponding to the SRB measure) is close to 1 as expected. The remaining eigenvalues are separated away from the unit circle.

The remaining eigenvalues in Figure 11 are restricted to a disk away from the unit circle, in line with expectations if one used a suitable anisotropic Banach space for the domain of \mathcal{L} [15]. While we work in $L^2(X, m)$, we train our estimate of \mathcal{L} on smooth functions, and it is likely that this restriction to smooth functions produces the spectral gap we see in Figure 11.

Solving the eigenequation (3.2) similarly to the previous example, we reconstruct the leading eigenfunction (corresponding to $\lambda = 1$), which represents the SRB measure; see Figure 12.

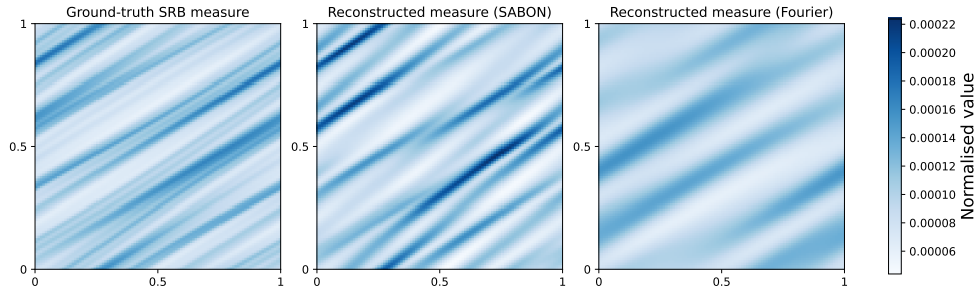


Fig. 12: Densities of ground-truth SRB measure (left), its reconstruction using the SABON learned basis (middle), and its reconstruction using a Fourier basis of the same dimension (right). We consider the densities as vectors on the grid and make their ℓ_1 -norms equal to 1.

The “ground truth” SRB measure is constructed from $N = 10\,000$ Fourier basis functions, with Fejér-kernel smoothing [9]. In comparison, our reconstructed SRB measure uses 225 learned basis functions. We also compare our learned SRB measure

with the SRB measure estimate arising from the lowest-order 225 Fourier modes. We use the real Fourier basis on $[0, 1]^2$ consisting of all modes with $k_1, k_2 \leq 7$. This gives us $15^2 = 225$ basis functions, where the factor of 15 comes from having one constant plus seven sine-cosine pairs in each dimension. Our reconstructed SRB measure using our learned basis clearly captures more detail and relevant dynamical structure than a high-quality basis created from a similar number of Fourier modes.

To quantitatively benchmark the learned basis against the traditional Fourier basis we measure both the relative L^2 error and Wasserstein W_1 distance of the orthogonally projected ground-truth SRB measure onto each basis. Letting \mathcal{B} denote either of the two bases, denote the orthogonal projector onto \mathcal{B} by $P_{\mathcal{B}} : L^2(X) \rightarrow \text{span}(\mathcal{B})$. Define the relative L^2 projection error

$$L_{\mathcal{B}}^{2,\text{rel}}(\rho_{\text{SRB}}, P_{\mathcal{B}}(\rho_{\text{SRB}})) := \frac{\|\rho_{\text{SRB}} - P_{\mathcal{B}}(\rho_{\text{SRB}})\|_2}{\|\rho_{\text{SRB}}\|_2}.$$

An SRB measure is typically a distribution and not a function, and therefore it has no density with respect to Lebesgue measure. This makes comparisons in the L^2 norm less meaningful (the L^2 topology is too strong). More appropriate is the 1-Wasserstein metric on probability measures. The 1-Wasserstein distance is defined as

$$W_1(\rho, \eta) := \inf_{\pi \in \Pi(\rho, \eta)} \int_{X \times X} d(x, y) \, d\pi(x, y),$$

where $d(x, y)$ is the metric distance between x and y on the phase space X and $\Pi(\rho, \eta)$ denotes all probability measures π on $X \times X$ whose first marginal is ρ and whose second marginal is η . After discretising ρ and η onto the uniform grid $\{x_i\}_{i=1, \dots, n}$, the infimum above can be written as the linear program

$$\min_{\pi \geq 0} \sum_{i,j=1}^n \pi_{ij} C_{ij} \quad \text{s.t.} \quad \sum_{j=1}^n \pi_{ij} = \rho_i, \quad \sum_{i=1}^n \pi_{ij} = \eta_j,$$

where C_{ij} is the distance between x_i and x_j in X for $i, j = 1, \dots, n$, π_{ij} is the mass flow between x_i and x_j , and $0 \leq \rho_i, \eta_i \leq 1$ are the discrete masses assigned by ρ, η (respectively) to the point $x_i \in X$ for each $i = 1, \dots, n$.

As in the relative L^2 norm calculation, we compute $W_1(\rho_{\text{SRB}}, P_{\mathcal{B}}(\rho_{\text{SRB}}))$ when (i) \mathcal{B} is the learned basis and (ii) \mathcal{B} is a Fourier basis of comparable cardinality. Table 5 shows that in both L^2 and Wasserstein distances, the learned SABON basis achieves the smallest error, which implies that the learned basis is able to better capture the detailed structure in the “ground truth” SRB distribution.

Table 5: Approximation error of the ground-truth SRB measure under orthogonal projection onto the two candidate bases. Lower values denote a more accurate representation.

Basis	$L_{\mathcal{B}}^{2,\text{rel}}(\rho_{\text{SRB}}, P_{\mathcal{B}}(\rho_{\text{SRB}}))$	$W_1(\rho_{\text{SRB}}, P_{\mathcal{B}}(\rho_{\text{SRB}}))$
SABON (225 functions)	7.479×10^{-2}	7.886×10^{-4}
Fourier (225 functions)	1.318×10^{-1}	1.717×10^{-3}

Finally, we quantify and compare the invariance of the subspaces generated by the learned basis and a classical Fourier basis of the same size under the action of the Perron–Frobenius operator. We compute principal angles between each subspace and its image under the operator, summarising these in Table 6. The significantly smaller distances obtained for our learned subspace indicate superior invariance compared with the traditional Fourier basis.

Table 6: Subspace-distance measures quantifying how well the subspace is preserved under the Perron–Frobenius operator, comparing the SABON basis (225 elements, no sparsity penalty) with a Fourier basis with 225 functions. Lower values indicate greater invariance.

Metric	SABON basis	Fourier basis
Geodesic (d_{\max})	0.037	16.642
Chordal (d_{ch})	0.037	10.615
Projection (d_{pr})	0.026	1.000

A more detailed comparison is shown graphically in Figure 13, where we plot the projection distance for every individual principal angle for both subspaces.

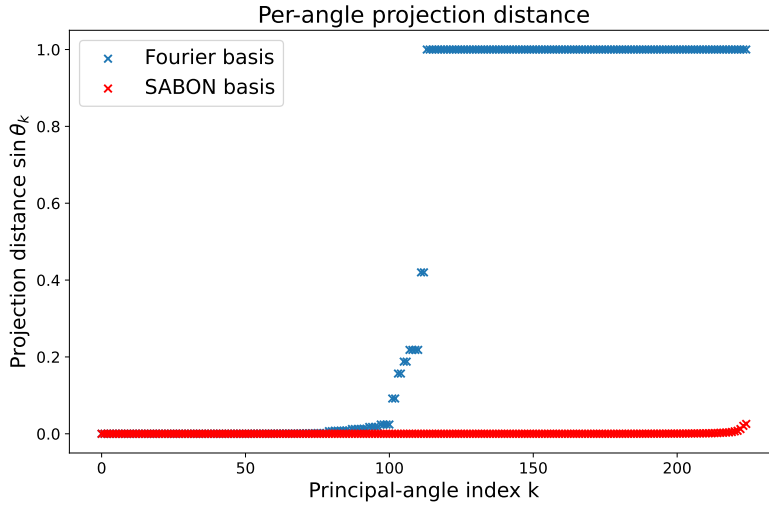


Fig. 13: Projection distance for the principal angles between each subspace and its image under the Perron–Frobenius operator for the learned basis and the Fourier basis of equal cardinality. Smaller distances correspond to greater invariance.

Why does the SABON basis have far superior invariance when compared to a Fourier basis? A Fourier element — whether the complex exponential $e^{2\pi i k \cdot x}$ or the purely real sine–cosine products introduced in subsection 3.1 — is aligned with coordinate axes. The contracting dynamics of T means that the frequency of a Fourier mode will be increased in stable directions of the dynamics under application of \mathcal{L} . Thus, those modes in the Fourier basis with higher frequencies may be pushed far out of the original span of the Fourier modes, and made near-orthogonal to the Fourier

basis. Indeed, Figure 13 indicates that this occurs to more than half of the Fourier modes.

The SABON basis, on the other hand, is learned jointly with the dynamics, so the network discovers functions that organise along the stable and unstable directions. The resulting modes resemble elongated ridges: smooth in the expanding direction and more sharply confined in the contracting one. When such a ridge is pushed forward by \mathcal{L} it tends to become another ridge, consistent with the invariance of the SABON subspace. This anisotropic feature, absent from the isotropic Fourier family, accounts for the much smaller distances reported for SABON in Table 6 and illustrated in Figure 13.

A further crucial aspect of our learned SABON basis is its *efficiency*. As mentioned above, our learned basis functions tend to align with the stable and unstable directions arising from the dynamics. This yields basis functions that have more rapid oscillation in stable directions and slower oscillation in unstable directions, which is exactly the form one expects for eigendistributions [15]. With a comparable number of basis functions, our learned functions can therefore more accurately represent the eigenprojectors.

4. Conclusions. We introduced the Single Autoencoder Basis Operator Network (SABON)—a neural framework that jointly learns

- an operator approximation $\hat{\mathcal{L}}$ of a Koopman or Perron–Frobenius operator \mathcal{L} and
- a data-driven basis $\{\phi_j\}_{j=1}^N$ whose span $V = \text{span}\{\phi_j\}_{j=1}^N$ is approximately invariant under \mathcal{L} .

SABON cleanly achieves this by combining an encoding–reconstruction structure with a linear latent map \mathcal{G} and a composite loss that balances operator approximation accuracy and sparsity. We proved a universal approximation theorem in the spirit of Hua [16], specialised to a single neural basis that targets transfer and Koopman operators.

Two canonical examples were used to highlight key features of SABON:

1. **Circle rotation.** The SABON-learned basis accurately reconstructed the analytic eigenpairs and recovered the rotation angle α directly from the leading eigenvalues, while the associated eigenfunctions coincided with the theoretical $e^{ik\theta}$ modes. Thus, the learned basis accurately captured the main dynamical properties.
2. **Perturbed Arnold’s cat map.** SABON’s learned basis outperformed a traditional Fourier basis for a nonlinear uniformly hyperbolic map by adapting to the geometry inherent in the dynamics. This is particularly surprising given the well-known theoretical approximation strengths of Fourier modes. The network discovered basis functions largely aligned with the contracting and expanding directions, leading to more accurate estimates of the physical invariant measure of the dynamics and a highly invariant approximation subspace.

SABON opens up new possibilities for constructing compact and accurate transfer and Koopman operator representations, particularly in difficult situations where isotropic bases fail and data-adaptive bases may excel. Moreover, SABON is in principle extendable to high-dimensional or partially observed systems. Future theoretical challenges include deriving quantitative rates that relate network width, depth, and sparsity to the operator approximation error.

Data availability. All code and data supporting our findings is publicly available

in our repository at <https://github.com/kevinkuhl/SABON>.

Acknowledgments. The research of GF is supported by an Australian Research Council (ARC) Laureate Fellowship FL230100088. The research of KK is supported by a UNSW University International Postgraduate Award, with additional funding from UNSW’s School of Mathematics and Statistics and the ARC Laureate Fellowship. Computational resources were generously provided by Katana infrastructure at UNSW [30], which significantly facilitated this research.

REFERENCES

- [1] A. AMINI, C. ZHENG, Q. SUN, AND N. MOTEE, *Carleman linearization of nonlinear systems and its finite-section approximations*, 2025, <https://doi.org/10.3934/dcdsb.2024102>, <https://www.aims sciences.org/article/id/66bb1050c19d0835a27a7ed7>.
- [2] H. ARBABI AND I. MEZIĆ, *Ergodic theory, dynamic mode decomposition, and computation of spectral properties of the Koopman operator*, SIAM Journal on Applied Dynamical Systems, 16 (2017), pp. 2096–2126, <https://doi.org/10.1137/17M1125236>, <https://doi.org/10.1137/17M1125236>, <https://arxiv.org/abs/https://doi.org/10.1137/17M1125236>.
- [3] K. BHATTACHARYA, B. HOSSEINI, N. B. KOVACHKI, AND A. M. STUART, *Model reduction and neural networks for parametric PDEs*, The SMAI Journal of Computational Mathematics, 7 (2021), pp. 121–157, <https://doi.org/10.5802/smai-jcm.74>, <https://smai-jcm.centre-mersenne.org/articles/10.5802/smai-jcm.74/>.
- [4] N. BOULLÉ AND A. TOWNSEND, *A mathematical guide to operator learning*, Elsevier, 2024, p. 83–125, <https://doi.org/10.1016/bs.hna.2024.05.003>, <http://dx.doi.org/10.1016/bs.hna.2024.05.003>.
- [5] R. BOWEN, *Equilibrium states and the ergodic theory of Anosov diffeomorphisms*, Lecture Notes in Mathematics, 470 (1975).
- [6] H. BREZIS AND H. BRÉZIS, *Functional analysis, Sobolev spaces and partial differential equations*, vol. 2, Springer, 2011.
- [7] S. L. BRUNTON, B. W. BRUNTON, J. L. PROCTOR, AND J. N. KUTZ, *Koopman invariant subspaces and finite linear representations of nonlinear dynamical systems for control*, PLOS One, 11 (2016), p. e0150171, <https://doi.org/10.1371/journal.pone.0150171>, <http://dx.doi.org/10.1371/journal.pone.0150171>.
- [8] T. CHEN AND H. CHEN, *Universal approximation to nonlinear operators by neural networks with arbitrary activation functions and its application to dynamical systems*, IEEE Transactions on Neural Networks, 6 (1995), pp. 911–917, <https://doi.org/10.1109/72.392253>.
- [9] H. CRIMMINS AND G. FROYLAND, *Fourier approximation of the statistical properties of Anosov maps on tori*, Nonlinearity, 33 (2020), pp. 6244–6296.
- [10] T. EISNER, B. FARKAS, M. HAASE, AND R. NAGEL, *Operator theoretic aspects of ergodic theory*, Springer International Publishing, 2015, <https://doi.org/10.1007/978-3-319-16898-2>, <http://dx.doi.org/10.1007/978-3-319-16898-2>.
- [11] G. FROYLAND, D. GIANNAKIS, B. R. LINTNER, M. PIKE, AND J. SLAWINSKA, *Spectral analysis of climate dynamics with operator-theoretic approaches*, Nature Communications, 12 (2021), <https://doi.org/10.1038/s41467-021-26357-x>, <http://dx.doi.org/10.1038/s41467-021-26357-x>.
- [12] D. GIANNAKIS, J. SLAWINSKA, AND Z. ZHAO, *Spatiotemporal feature extraction with data-driven Koopman operators*, in Proceedings of the 1st International Workshop on Feature Extraction: Modern Questions and Challenges at NIPS 2015, D. Storcheus, A. Rostamizadeh, and S. Kumar, eds., vol. 44 of Proceedings of Machine Learning Research, Montreal, Canada, 11 Dec 2015, PMLR, pp. 103–115, <https://proceedings.mlr.press/v44/giannakis15.html>.
- [13] C. GIN, B. LUSCH, S. L. BRUNTON, AND J. N. KUTZ, *Deep learning models for global coordinate transformations that linearise PDEs*, European Journal of Applied Mathematics, 32 (2021), p. 515–539, <https://doi.org/10.1017/S0956792520000327>.
- [14] G. H. GOLUB AND C. F. VAN LOAN, *Matrix computations*, JHU Press, 2013.
- [15] S. GOUËZEL AND C. LIVERANI, *Banach spaces adapted to Anosov systems*, Ergodic Theory and dynamical systems, 26 (2006), pp. 189–217.
- [16] N. HUA AND W. LU, *Basis operator network: a neural network-based model for learning nonlinear operators via neural basis*, Neural Networks, 164 (2023), pp. 21–37, <https://doi.org/https://doi.org/10.1016/j.neunet.2023.04.017>, <https://www.sciencedirect.com/science/article/pii/S0893608023002034>.

- [17] C. A. JOHNSON, S. BALAKRISHNAN, AND E. YEUNG, *Heterogeneous mixtures of dictionary functions to approximate subspace invariance in Koopman operators*, 2022, <https://doi.org/10.48550/ARXIV.2206.13585>, <https://arxiv.org/abs/2206.13585>.
- [18] C. A. JOHNSON, S. BALAKRISHNAN, AND E. YEUNG, *Heterogeneous mixtures of dictionary functions to approximate subspace invariance in Koopman operators: why deep Koopman operators work*, *Journal of Nonlinear Science*, 35 (2025), <https://doi.org/10.1007/s00332-025-10159-2>, <http://dx.doi.org/10.1007/s00332-025-10159-2>.
- [19] S. KLUS, F. NÜSKE, P. KOLTAI, H. WU, I. KEVREKIDIS, C. SCHÜTTE, AND F. NOÉ, *Data-driven model reduction and transfer operator approximation*, *Journal of Nonlinear Science*, 28 (2018), pp. 985–1010, <https://doi.org/10.1007/s00332-017-9437-7>, <https://doi.org/10.1007/s00332-017-9437-7>.
- [20] A. V. KNYAZEV AND M. E. ARGENTATI, *Principal angles between subspaces in an A-based scalar product: algorithms and perturbation estimates*, *SIAM Journal on Scientific Computing*, 23 (2002), p. 2008–2040, <https://doi.org/10.1137/S1064827500377332>, <http://dx.doi.org/10.1137/S1064827500377332>.
- [21] B. O. KOOPMAN, *Hamiltonian systems and transformation in Hilbert space*, *Proceedings of the National Academy of Sciences*, 17 (1931), pp. 315–318, <https://doi.org/10.1073/pnas.17.5.315>, <https://www.pnas.org/doi/abs/10.1073/pnas.17.5.315>, <https://arxiv.org/abs/https://www.pnas.org/doi/pdf/10.1073/pnas.17.5.315>.
- [22] N. KOVACHKI, Z. LI, B. LIU, K. AZIZZADENESHELI, K. BHATTACHARYA, A. STUART, AND A. ANANDKUMAR, *Neural operator: learning maps between function spaces with applications to PDEs*, *Journal of Machine Learning Research*, 24 (2023).
- [23] H.-G. LEE, *Linearization of nonlinear control systems*, Springer Nature Singapore, 2022, <https://doi.org/10.1007/978-981-19-3643-2>, <http://dx.doi.org/10.1007/978-981-19-3643-2>.
- [24] Q. LI, F. DIETRICH, E. M. BOLLT, AND I. G. KEVREKIDIS, *Extended dynamic mode decomposition with dictionary learning: a data-driven adaptive spectral decomposition of the Koopman operator*, *Chaos: An Interdisciplinary Journal of Nonlinear Science*, 27 (2017), p. 103111, <https://doi.org/10.1063/1.4993854>, <https://doi.org/10.1063/1.4993854>, https://arxiv.org/abs/https://pubs.aip.org/aip/cha/article-pdf/doi/10.1063/1.4993854/13247075/103111_1.online.pdf.
- [25] Z. LI, N. KOVACHKI, K. AZIZZADENESHELI, B. LIU, K. BHATTACHARYA, A. STUART, AND A. ANANDKUMAR, *Fourier neural operator for parametric partial differential equations*, 2020, <https://doi.org/10.48550/ARXIV.2010.08895>, <https://arxiv.org/abs/2010.08895>.
- [26] L. LU, P. JIN, G. PANG, Z. ZHANG, AND G. E. KARNIADAKIS, *Learning nonlinear operators via DeepONet based on the universal approximation theorem of operators*, *Nature Machine Intelligence*, 3 (2021), p. 218–229, <https://doi.org/10.1038/s42256-021-00302-5>, <http://dx.doi.org/10.1038/s42256-021-00302-5>.
- [27] B. LUSCH, J. N. KUTZ, AND S. L. BRUNTON, *Deep learning for universal linear embeddings of nonlinear dynamics*, *Nature Communications*, 9 (2018), p. 4950, <https://doi.org/10.1038/s41467-018-07210-0>, <https://doi.org/10.1038/s41467-018-07210-0>.
- [28] I. MEZIĆ, *Analysis of fluid flows via spectral properties of the Koopman operator*, *Annual Review of Fluid Mechanics*, 45 (2013), p. 357–378, <https://doi.org/10.1146/annurev-fluid-011212-140652>, <http://dx.doi.org/10.1146/annurev-fluid-011212-140652>.
- [29] S. E. OTTO AND C. W. ROWLEY, *Linearly recurrent autoencoder networks for learning dynamics*, *SIAM Journal on Applied Dynamical Systems*, 18 (2019), pp. 558–593, <https://doi.org/10.1137/18M1177846>, <https://doi.org/10.1137/18M1177846>, <https://arxiv.org/abs/https://doi.org/10.1137/18M1177846>.
- [30] PVC (RESEARCH INFRASTRUCTURE), UNSW SYDNEY, *Katana*, 2010, <https://doi.org/10.26190/669X-A286>, <https://researchdata.edu.au/katana/1733007>.
- [31] P. J. SCHMID, *Dynamic mode decomposition of numerical and experimental data*, *Journal of Fluid Mechanics*, 656 (2010), p. 5–28, <https://doi.org/10.1017/S0022112010001217>.
- [32] H. SHI AND M. Q.-H. MENG, *Deep Koopman operator with control for nonlinear systems*, *IEEE Robotics and Automation Letters*, 7 (2022), pp. 7700–7707, <https://doi.org/10.1109/LRA.2022.3184036>.
- [33] N. TAKEISHI, Y. KAWAHARA, AND T. YAIRI, *Learning Koopman invariant subspaces for dynamic mode decomposition*, in *Advances in Neural Information Processing Systems*, I. Guyon, U. V. Luxburg, S. Bengio, H. Wallach, R. Fergus, S. Vishwanathan, and R. Garnett, eds., vol. 30, Curran Associates, Inc., 2017, https://proceedings.neurips.cc/paper_files/paper/2017/file/3a835d3215755c435ef4fe9965a3f2a0-Paper.pdf.
- [34] M. O. WILLIAMS, I. G. KEVREKIDIS, AND C. W. ROWLEY, *A data-driven approximation of the Koopman operator: extending dynamic mode decomposition*, *Journal of Nonlinear Science*, 25 (2015), p. 1307–1346, <https://doi.org/10.1007/s00332-015-9258-5>, <http://dx.doi.org/10.1007/s00332-015-9258-5>.

- 10.1007/s00332-015-9258-5.
- [35] E. YEUNG, S. KUNDU, AND N. HODAS, *Learning deep neural network representations for Koopman operators of nonlinear dynamical systems*, in 2019 American Control Conference (ACC), 2019, pp. 4832–4839, <https://doi.org/10.23919/ACC.2019.8815339>.